

This work has been submitted to the Springer for possible publication. Copyright may be transferred without notice, after which this version may no longer be accessible.

arXiv:2507.05979v1 [cs.RO] 8 Jul 2025

AURA-CVC: Autonomous Ultrasound-guided Robotic Assistance for Central Venous Catheterization

Deepak Raina¹, Lidia Al-Zogbi¹, Brian Teixeira², Vivek Singh²,
Ankur Kapoor², Thorsten Fleiter³, Muyinatu A. Lediju Bell^{1†},
Vinciya Pandian^{4†}, Axel Krieger^{1*†}

¹Johns Hopkins University, Baltimore, MD, USA.

²Siemens Healthineers, Princeton, NJ, USA.

³University of Maryland, Baltimore, MD, USA.

⁴Penn State University, University Park, PA, USA.

*Corresponding author(s). E-mail(s): axel@jhu.edu;

†These authors advised this work equally.

Abstract

Purpose: Central venous catheterization (CVC) is a critical medical procedure for vascular access, hemodynamic monitoring, and life-saving interventions. Its success remains challenging due to the need for continuous ultrasound-guided visualization of a target vessel and approaching needle, which is further complicated by anatomical variability and operator dependency. Errors in needle placement can lead to life-threatening complications. While robotic systems offer a potential solution, achieving full autonomy remains challenging. In this work, we propose an end-to-end robotic-ultrasound-guided CVC pipeline, from scan initialization to needle insertion.

Methods: We introduce a deep-learning model to identify clinically relevant anatomical landmarks from a depth image of the patient’s neck, obtained using RGB-D camera, to autonomously define the scanning region and paths. Then, a robot motion planning framework is proposed to scan, segment, reconstruct, and localize vessels (veins and arteries), followed by the identification of the optimal insertion zone. Finally, a needle guidance module plans the insertion under ultrasound guidance with operator’s feedback. This pipeline was validated on a high-fidelity commercial phantom across 10 simulated clinical scenarios.

Results: The proposed pipeline achieved 10 out of 10 successful needle placements on the first attempt. Vessels were reconstructed with a mean error of 2.15 *mm*,

and autonomous needle insertion was performed with an error less than or close to 1 *mm*.

Conclusion: To our knowledge, this is the first robotic CVC system demonstrated on a high-fidelity phantom with integrated planning, scanning, and insertion. Experimental results show its potential for clinical translation.

Keywords: Robotic ultrasound, ultrasound-guided interventions, central venous catheterization, motion-planning

1 Introduction

Central venous catheterization (CVC) is a critical procedure used in intensive care, trauma resuscitation, major surgeries, parenteral nutrition delivery, and hemodialysis. Over 7 million CVCs are placed annually in the U.S. alone [1]. It is typically performed at one of three primary sites: the internal jugular (IJ), subclavian, or femoral veins, with IJ as a preferred site due to its superficial location, consistent anatomy, and lower complication risk. Moreover, ultrasound-guided CVC has become clinical standard due to its improved safety [2]. The procedure begins with scanning the target region via ultrasound to identify vessels, followed by estimating the insertion point and needle trajectory. Major complications are observed in approximately 3% of 1000 CVC placements, with rates reported as ~ 4.4 for pneumothorax, ~ 16.2 for arterial puncture, and ~ 2.8 for arterial cannulation [3]. Although ultrasound guidance reduces complications, maintaining continuous visualization of both the vessel and advancing needle in the narrow imaging plane remains a major challenge [4]. Even experienced practitioners have to carefully balance probe positioning and needle advancement. These challenges highlight the need for advanced technologies to reduce workload and improve safety.

Robot-assisted ultrasound (RUS) has emerged as a promising solution to enhance precision, minimize human error, and improve procedural outcomes in various diagnostic and interventional applications [5–7]. Several handheld and semi-automated needle insertion devices have been developed to optimize workspace, accuracy, and force resistance [8–10]. Among them, CathBot [10] allows clinicians to initiate insertion by pushing a handle, with the device completing cannulation autonomously. While this was effective for peripheral vascular access procedures on forearm, it has limitations in CVC due to anatomical complexities at neck, chest, or groin insertion sites. Later, the focus shifted towards enhancing the dexterity of these mechanisms using advanced robotics, imaging, and sensor guidance for needles. Hong *et al.* [11] proposed a percutaneous needle insertion robot that can compensate for involuntary patient motion using real-time visual-servoing. Neubach *et al.* [12] presented a closed-loop robotic controller for flexible needle steering by calculating the needle tip position from ultrasound images, while accounting for tissue displacement from a stiffness model. Xu *et al.* [13] proposed a slice guidance method, which interpolated preoperative scans in real-time to compensate for the motion of liver during needle placement. Chatelain

et al. [14] used particle filtering to track the flexible needle for real-time closed-loop control during targeting. While these approaches [11–14] demonstrate promising closed-loop control and organ motion compensation techniques, they lack integrated intra-operative planning for a fully autonomous procedure.

Zetting *et al.* [15] annotated pre-interventional plans in CT/MRI and proposed a 3D visual servoing framework with multi-modal registration to dynamically update the needle target with anatomical motion. Kojcev *et al.* [16] developed a dual-arm ultrasound-guided system integrating force-controlled image acquisition, registration, vision-based control, and needle tracking. However, intra-operative planning still relied on manual region selection. Bell *et al.* [17] and Gubbi *et al.* [18] demonstrated photoacoustic-based (rather than ultrasound) visual servoing of needle. Cheng *et al.* [19] used electrical impedance sensing to detect vascular entry. In these cases, no intra-operative planning with CT or MRI registration was used. Koskinopoulou *et al.* [20] combined ultrasound and bioimpedance in a dual-arm system for robust vessel localization and venipuncture detection. While the above-discussed systems [15–20] successfully demonstrated end-to-end procedures, scanning was either initialized from a predefined pose or relied on medical experts to manually review intra-operative CT/MRI images.

In contrast, our system achieves fully autonomous scan initialization using feedback from a low-cost, widely accessible RGB-D camera, eliminating the need for expert intervention or expensive intra-operative imaging. In addition, many of the initial system validations were performed with simplified vascular access phantoms that do not capture the anatomical and physiological complexity of humans. In this work, we validate our initial pipeline on a high-fidelity phantom model, moving one step closer to in-human procedures. **Key contributions** of this work include:

1. An end-to-end robotic pipeline to perform key CVC steps: intra-operative planning, scanning, anatomical localization, and needle placement.
2. A method to predict the optimal scanning region and trajectory using only a depth image from an RGB-D camera.
3. Automated robotic scanning and vascular reconstruction for localization of vein and artery, followed by supervised needle guidance.
4. Validation on a near-realistic CVC phantom for IJ vein access across 10 diverse clinical scenarios.

2 Materials and Methods

2.1 Experimental testbed

The experimental testbed (Fig. 1) includes: (1) a 6–DoF UR10e robotic arm (Universal Robots, Denmark) with 10 kg payload and inbuilt force-torque sensor, (2) a C3 HD3 curved ultrasound probe (Clarius, Canada) mounted via an extended attachment for real-time imaging. Although linear probes are preferred for CVC, we used a convex probe for its wider field of view and availability during prototyping. (3) An Ubuntu PC and a laptop, with NVIDIA RTX 4090 (16GB) and 1090 (12GB) for system control and deep learning inferences, respectively, (4) an Intel RealSense D415 RGB-D

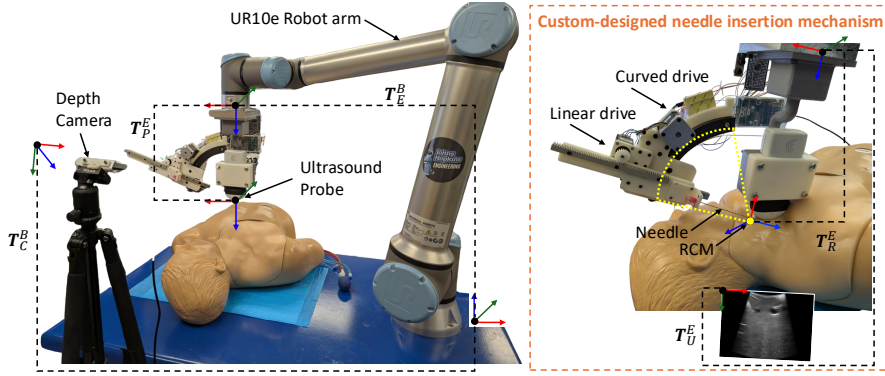


Fig. 1 Overview of the experimental testbed showing the robotic system setup, a close-up view of the needle insertion mechanism, and the defined reference frames. The corresponding homogeneous transformation matrices, denoted as \mathbf{T}_1^2 , represent the pose of frame 1 relative to frame 2.

camera (California, USA) for spatial localization, (5) a custom 2-DoF needle insertion mechanism, adapted from the design in [21], providing linear and angular control, compatible with any robotic arm with adequate payload capacity, and equipped with an 18-gauge, 15 cm percutaneous thin-wall bevel-tipped needle (Cook Medical, USA), (6) The CVC Blue Phantom (CAE, USA) for validation, offering highly realistic upper thorax and neck anatomy, including major vessels and anatomical landmarks commonly used in CVC. Note that the communication across all components of the setup is established via ROS2 (Robot Operating System).

Let \mathbf{T}_1^2 denote the homogeneous transformation matrix that expresses the pose of frame 1 relative to frame 2. The frames used in the system are: robot's base frame (B), end-effector (E), camera (C), probe tip (P), remote center-of-motion (R), and ultrasound image (U) (see Fig. 1). The 3D position in world coordinate system (p_B) of a given pixel in the 2D ultrasound image (p_I) is calculated using:

$$\mathbf{p}_B = \mathbf{T}_E^B \cdot \mathbf{T}_U^E \cdot \mathbf{T}_I^U \cdot \mathbf{p}_I \quad (1)$$

where \mathbf{T}_U^I is the transformation from the ultrasound image origin (top left corner) to the pixel values in the image and is given by

$$\mathbf{T}_U^I = \begin{bmatrix} S_x & 0 & 0 & 0 \\ 0 & S_y & 0 & 0 \\ 0 & 0 & 1 & 0 \\ 0 & 0 & 0 & 1 \end{bmatrix} \begin{bmatrix} I_x \\ I_y \\ 0 \\ 1 \end{bmatrix} \quad (2)$$

where $S_x = S_y = 0.15436 \text{ mm}$ is the pixel spacing (scaling factor) provided by the Clarius Mobile Health software development kit and (I_x, I_y) is the given pixel value in x - and y -direction of the image.

2.2 Pipeline

Our pipeline is shown in Fig. 2. During initialization, system calibration was performed by estimating T_C^B via hand-eye calibration and T_U^E using the classical $AX = XB$ method [22], with a cross-wire phantom in a water bath. The IJ vein and carotid artery region was then autonomously identified from depth images, followed by robotic ultrasound scanning, vessel segmentation, 3D reconstruction, insertion point selection, and closed-loop needle guidance for puncture.

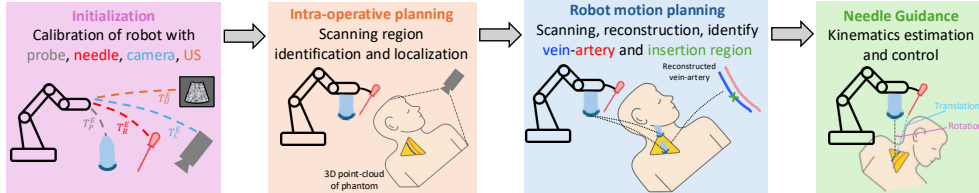


Fig. 2 Our pipeline has four phases: the initialization phase, intra-operative planning, robot motion planning, and the needle guidance

2.3 Intra-operative planning

Clinicians often define a triangular region using the suprasternal notch (SN), sternocleidomastoid (SCM) midpoint, and lateral clavicle (LC), known as Sedillot’s triangle, to guide IJ vein access [23]. Inspired by this, we used SN, LC, and anterior hyoid bone tip (HT) to define a similar region, with HT chosen for its prominence and absence of SCM in the phantom. This region still ensured IJ vein’s presence. To identify these landmarks, we used a Dense-UNet deep learning model, as described below.

2.3.1 Anatomical landmark prediction network

The anatomical landmark prediction network required a depth image of neck and torso region of the body to predict the landmarks. First, a synchronized depth and color images of the environment was captured by the depth camera. An HSV-based thresholding then segmented the region-of-interest i.e. phantom’s head and torso, followed by depth filtering for a refined 3D point cloud. The segmented ROI point cloud was provided as input to the network, as shown in Fig. 3(a).

Following the approach in [24], we trained a Dense-UNet [25] to predict the location of internal landmarks from computed depth images. The network architecture consisted of an encoder and decoder, each with four dense blocks of four convolutional layers (Fig. 3(b)). Batch normalization and ReLU activation were applied after each convolutional layer, except for the final layer. The dataset of 4,912 depth images was used to train the Dense-UNet model, consisting of real human subjects with diverse body habitus, sex, and skin tone profiles. Each image was paired with manually annotated 3D anatomical landmarks by trained technicians using co-registered RGB-D data and verified against physical anthropometric measurements to ensure accuracy.

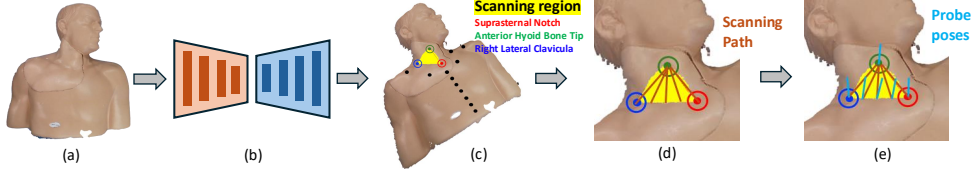


Fig. 3 (a) Depth image of the phantom’s neck and torso. (b) Landmark prediction network for anatomical localization. (c) Scanning region (yellow patch) on the neck is defined using three predicted anatomical landmarks. (d) Planned scanning paths are shown as maroon lines. (e) Probe poses along the scanning paths, with surface normals at each pose illustrated by light-blue lines.

The network was trained for 300 epochs, minimizing the Adaloss function using the using the Adam optimizer (learning rate = 0.001, batch size = 32). The network predicted 33 landmarks, using additional ones for regularization to enhance accuracy of the 3 landmarks critical to CVC.

2.3.2 Scanning region and path estimation

The scanning region was defined by triangular region formed by 3 predicted landmarks (SN, LC, and HT). This region was projected onto the phantom surface using the Open3D Python library, as shown in Fig. 3(c). To scan within this region, we defined straight-line paths from the triangle’s base (SN–LC) to its apex (HT), aligning with the IJ vein’s orientation. Initial paths connected HT to LC and HT to SN. Additional scanning paths were created by dividing the SN–LC line into equal intervals and connecting lines from HT to these points, yielding a dense scan pattern for accurate vessel detection (Fig. 3(d)). Scanning was initiated along the midpoint-to-HT path because this path aligned with the expected anatomical course of the IJ vein, offering a clinically representative initial view. Additionally, it provided a reliable starting point across different patient positioning due to its geometric symmetry.

2.4 Robot motion planning

Once the scanning region was identified, the pipeline generated a robot trajectory for scanning and localizing the vein-artery, as illustrated in Fig. 4. After robotic scanning, the vein was localized and centered in the ultrasound image to ensure consistent spatial referencing. Then the robot was re-oriented for sagittal plane insertion, as it offered full needle shaft visibility. A collision check was performed using the CAD model and phantom point cloud. If a collision was detected in the sagittal orientation, the robot iteratively adjusted its pivot angle in transverse view about the point of contact by 5° until a collision-free pose was found. Upon confirming clearance, the robot transitioned to the sagittal plane for needle insertion.

2.4.1 Scanning trajectory

The scanning path generated on the phantom in Section 2.3 defined the robot trajectory as:

$$\mathcal{T} = [P_i, \dots, P_n] \quad (3)$$

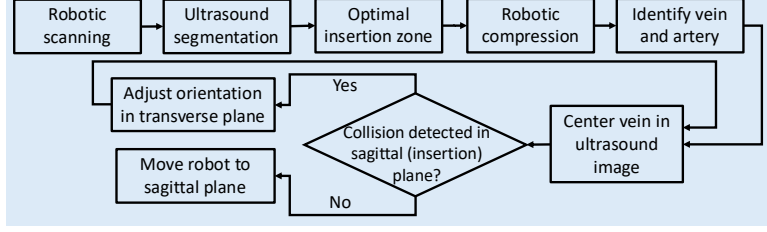


Fig. 4 Robot motion planning workflow to identify optimal insertion point, localize vein-artery, and move to sagittal (insertion) plane while avoiding collision.

Each pose transform \mathbf{P}_* is defined as $[\vec{x}, \vec{y}, \vec{z}, \vec{t}]$, where \vec{t} is the translation (or position) vector and $\vec{x}, \vec{y}, \vec{z}$ are unit vectors for orientation. The start and end of the scanning path define \mathbf{P}_0 and \mathbf{P}_n , respectively. The normal \vec{z} of phantom was computed using Open3D and aligned with the end-effector’s normal \vec{z}_e using:

$$\vec{z} = \begin{cases} \vec{z}, & \text{if } \vec{z} \cdot \vec{z}_e > 0 \\ -\vec{z}, & \text{otherwise} \end{cases} \quad (4)$$

The x-axis \vec{x} was aligned with the phantom’s major axis, and \vec{y} was computed as:

$$\vec{y} = \frac{\vec{z} \times \vec{x}}{\|\vec{z} \times \vec{x}\|} \quad (5)$$

Intermediate poses were interpolated between \mathbf{P}_0 and \mathbf{P}_n using the UR driver. ROS2 and URScript executed the trajectory in hybrid force-position mode with $5N$ force along the probe’s z -axis. During scanning, a rosbag recorded poses and images pairs $(\mathbf{P}_i, \mathbf{I}_i)$ for each frame, as given in eq. (6), to enable accurate vessel reconstruction.

$$\mathbf{D} = \{(\mathbf{P}_i, \mathbf{I}_i), \dots, (\mathbf{P}_n, \mathbf{I}_n)\} \quad (6)$$

2.4.2 Identifying optimal insertion plane

The acquired 2D US frames were segmented to reconstruct vessels and plan needle insertion. A deep learning model from prior work [26] was used to extract vessel center-points and areas from each frame. Ideally, insertion should occur where both vessels (vein and artery) are clearly visible for confident and precise targeting. To determine this, the robot insertion pose (\mathcal{P}) was selected from $\mathbf{P}_i, \dots, \mathbf{P}_n$ as the one corresponding to the maximum combined area of the two vessels. This selection criterion is illustrated in Fig. 5. The robot was finally moved to pose \mathcal{P} , and the corresponding ultrasound frame was re-segmented.

2.4.3 Vein-artery localization

Veins are difficult to distinguish from arteries, as both appear morphologically similar in ultrasound images. While clinicians typically use Doppler ultrasound to differentiate them based on blood flow, this method requires manual tuning, favorable imaging

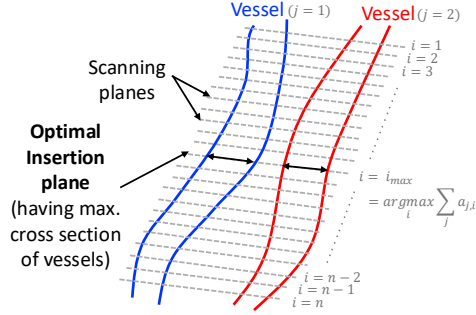


Fig. 5 Criteria for selecting optimal needle insertion plane. $a_{j,i}$ is the area of the j^{th} vessel in image I_i from dataset \mathcal{D} (Eq. (6)), with j limited to 2 to exclude noise, as only two vascular structures are expected to be visible.

conditions, and expertise, making it less practical in portable or low-cost devices where Doppler functionality or detectable flow is absent. To address this, our system employs a compression-based method that exploits differences in vascular compliance, whereby veins exhibit greater deformation than arteries under low external pressure.

The robot applied controlled compression by gradually increasing the contact force from 5 N to 10 N, then decreasing it back to 5 N, while recording an ultrasound video. Segmented vessel areas and centroids were extracted from the recorded sequence. Then, KMeans clustering was used, which grouped vessel centroids into two clusters based on their spatial proximity. Area changes across the compression cycle were computed for each cluster, with the one showing greater deformation identified as the vein, and the other as the artery. The centroid of the vein cluster was stored as a reference. Later, at the insertion pose, the robot captured a new ultrasound frame, segmented the vessels, and identified the vein by finding the centroid closest to the saved reference, with the remaining vessel labeled as the artery.

2.5 Needle guidance

The needle insertion parameters, angle (θ) and depth (d), are calculated by estimating the kinematic relation between the vein center and remote center-of-motion (RCM, see Fig. 1). The vein center is initially identified in the transverse ultrasound view, but remains at the same pixel location in the sagittal ultrasound view. Let $p^{VC} = [x^{VC}, y^{VC}, z^{VC}]$ and $p^{RCM} = [x^{RCM}, y^{RCM}, z^{RCM}]$ be the 3D position of IJ vein center and RCM in robot base frame, respectively. The variables θ and d can then be estimated using:

$$\theta = \tan^{-1} \left(\frac{\mathbf{x}^{VC} - \mathbf{z}^{RCM}}{|\mathbf{x}^{VC} - \mathbf{z}^{RCM}|} \right) - \theta_{offset} \quad (7)$$

$$d = \|\mathbf{p}^{VC} - \mathbf{p}^{RCM}\| \quad (8)$$

where, θ_{offset} is the initial angular offset of the needle (18.21°) due to the design constraints of the mechanism. To minimize targeting error, we implemented a closed-loop controller that minimizes the distance between the needle tip and the vein centerline

during advancement. As the needle angle couldn't be adjusted after insertion, the controller was primarily employed to minimize the distance between the needle tip and vein centerline during insertion. The controller used a proportional gain of 0.5 and required manual marking of the vein centerline (one-time) and needle tip (multiple-times) in sagittal ultrasound view after each step. Needle advancement was stopped when the tip is within 1 *mm* of the centerline.

3 Experiments and Results

To comprehensively evaluate the robustness and clinical relevance of our system, we conducted 10 experiments under varied simulated clinical scenarios. These included: (i) five experiments (Exp. 1-5) with different phantom orientations representing common patient positions during CVC (e.g., Trendelenburg, head turns, torso tilt); and (ii) five additional experiments (Exp. 6-10) introducing random perturbations by adding Gaussian noise ($\mu = 0, \sigma = 0.01$) to the scanning path to simulate real-world uncertainties such as patient motion or breathing. Fig. 6 illustrates the five baseline orientations, while Table 1 summarizes the corresponding phantom-to-robot frame transformations and noise-induced deviations.

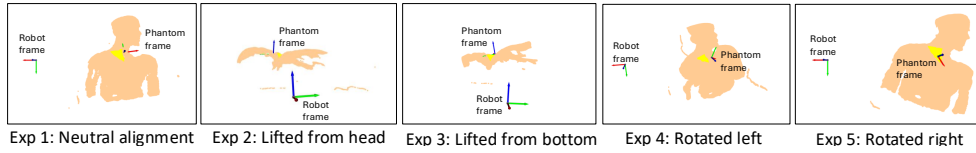


Fig. 6 Illustrating experiments 1–5, each with a different phantom orientation relative to the robot base to assess system’s robustness to patient positioning in different clinical scenarios.

Table 1 Exp. 1-5 corresponds to scenarios with different orientations (in *deg.*) of phantom with respect to (w.r.t) robot base and Exp. 6-10 corresponds to scenarios with different amounts of deviations (in *mm*) added to the start and end point of the scanning path.

Exp.	Rotation of phantom w.r.t robot			Exp.	Start Deviation		End Deviation	
	Roll	Pitch	Yaw		Δx	Δy	Δx	Δy
1	-3.220	-1.711	-173.129	6	+3.295	-4.298	-8.128	+7.024
2	6.011	-0.376	-177.914	7	+5.385	-17.523	+23.160	-5.776
3	13.003	-0.065	-174.284	8	+3.024	-5.065	-9.509	+1.549
4	4.036	-1.779	122.572	9	-1.270	+6.466	-1.229	-16.543
5	3.016	3.377	155.136	10	-10.250	+6.343	-2.225	-15.113

3.1 Landmark prediction

With 427 test depth images, the mean Euclidean error for 33 landmarks was 13.59 *mm* \pm 10.49 *mm* (95th percentile: 34.26 *mm*). For the three key CVC landmarks, SN,

RLC, and HT, the mean error was $13.88 \text{ mm} \pm 11.55$ (95th percentile: 35.35 mm). Table 2 shows detailed results. Although the maximum error reached 34.17 mm , it did not hinder downstream vessel localization, as the triangular scanning region was large enough to encompass the IJ vein in all cases. Nonetheless, reducing this error could improve accuracy in anatomically complex patients.

Table 2 Mean, standard deviation (S.D.), and 95th percentile error for CVC landmarks.

Landmark	Mean \pm S.D. (95 th Percentile) [mm]
SN	13.03 ± 11.21 (36.96)
RLC	12.77 ± 10.52 (32.09)
HT	15.84 ± 12.91 (37.01)
Average	13.88 ± 11.55 (35.35)

3.2 Vein-artery centerline reconstruction

We compared the reconstructed centerline with the ground truth center line obtained from CT scans of the phantom. The CT data was processed using the Vascular Modeling Toolkit in 3D Slicer to extract the centerlines discretized at 1 mm intervals to

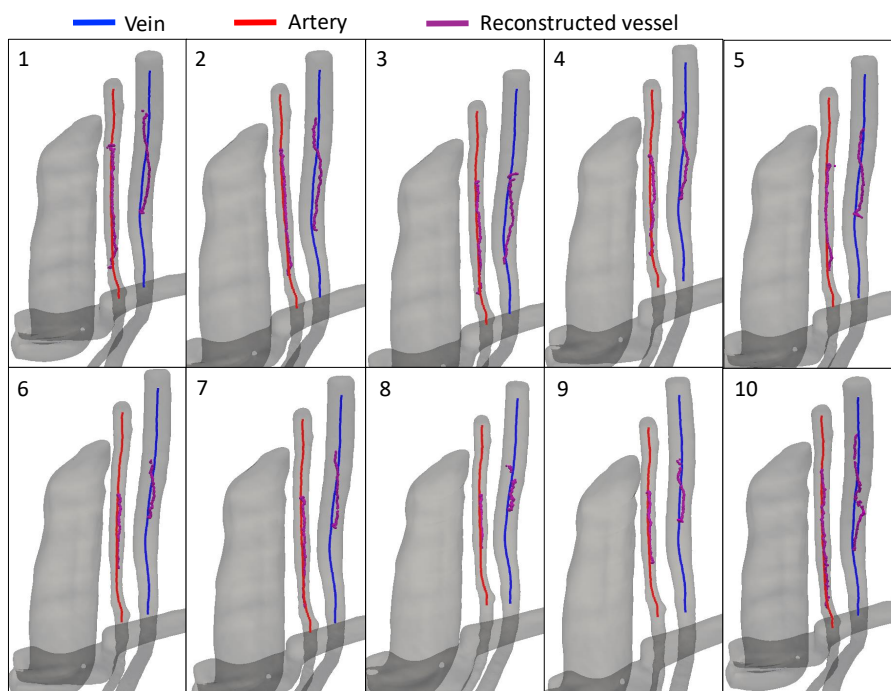


Fig. 7 Comparison of 3D reconstruction of centerline of vein and artery (both marked with magenta color) with their ground truths (blue color for vein and red color for artery) for the 10 experiments

serve as the ground truth. The reconstructed and ground truth centerlines were aligned using the ICP algorithm (Fig. 7). To assess the accuracy of reconstructed centerlines, we computed their k -nearest neighbors distance with the ground truth center-points and results are given in Table 3.

Table 3 Reconstruction accuracy reported as mean, maximum, and standard deviation (S.D.) errors (in mm) between reconstructed and ground-truth vein and artery center-lines.

Exp.	Vein			Artery		
	Mean	Max.	S.D.	Mean	Max.	S.D.
1	3.28	5.06	0.98	1.21	2.24	0.43
2	3.13	5.05	0.96	1.05	2.49	0.47
3	2.74	4.56	0.78	1.08	2.49	0.39
4	3.32	4.93	0.96	1.20	2.32	0.44
5	3.28	5.21	1.14	1.01	3.74	0.57
Avg (1-5)	3.15	4.96	0.96	1.11	2.66	0.46
6	3.28	4.94	0.80	1.01	2.77	0.44
7	3.29	4.57	0.87	1.02	2.05	0.32
8	3.10	6.12	1.23	1.08	2.46	0.51
9	3.38	4.26	0.54	1.08	1.79	0.28
10	3.33	5.71	0.88	1.19	3.16	0.45
Avg (6-10)	3.28	5.12	0.86	1.08	2.45	0.40

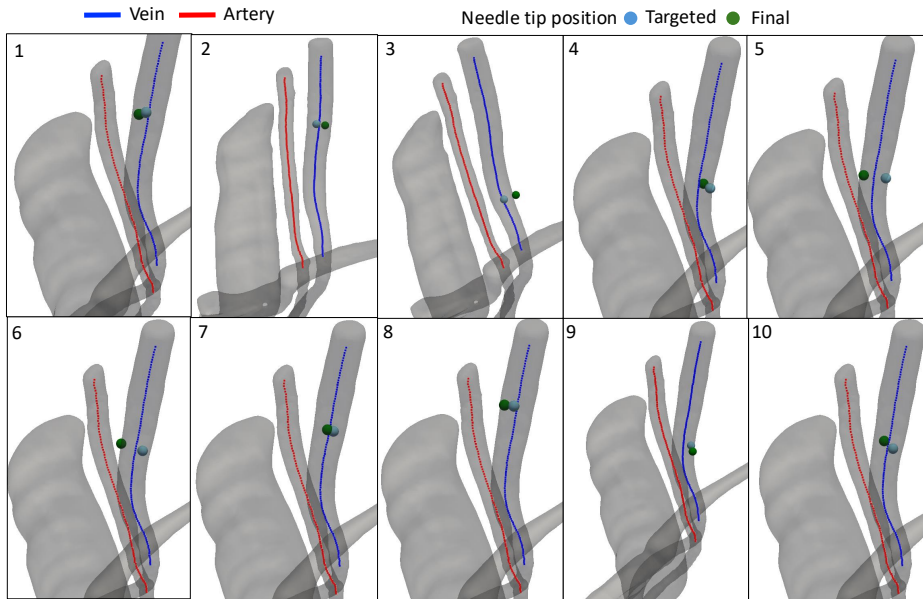


Fig. 8 Comparing the 3D needle tip position (green sphere) with the targeted vein center-point (blue sphere)

3.3 Needle targeting accuracy

The targeting accuracy of the system was evaluated by computing the error between the target and final needle tip position. To obtain these measurements, the 3D positions of the targeted point and needle tip were first calculated using eq. (1) from the marked pixel locations in the acquired sagittal view. At the conclusion of each experiment, an expert (co-author VP) evaluated the ultrasound frame and marked the observed needle location and IJ vein (its center point and elliptical boundary). This evaluation was first done in the sagittal ultrasound view after insertion. Then, the ultrasound probe was removed from the robot and manual hand-held scanning was performed to collect the transverse and sagittal ultrasound views from the insertion region. The catheter insertion was also performed to confirm the successful access to the punctured vein. Ultrasound videos were recorded during hand-held scanning and catheter insertion, which were later analyzed by the expert to confirm the safe insertion of the needle and catheter in the IJ Vein for each experiment. Fig. 8 shows the targeted 3D position inside the IJ vein and the final needle tip position after insertion. Table 4 summarizes the corresponding error between the needle tip and vein, both from its center-point and center-line, under the 'Evaluation via Robot' column.

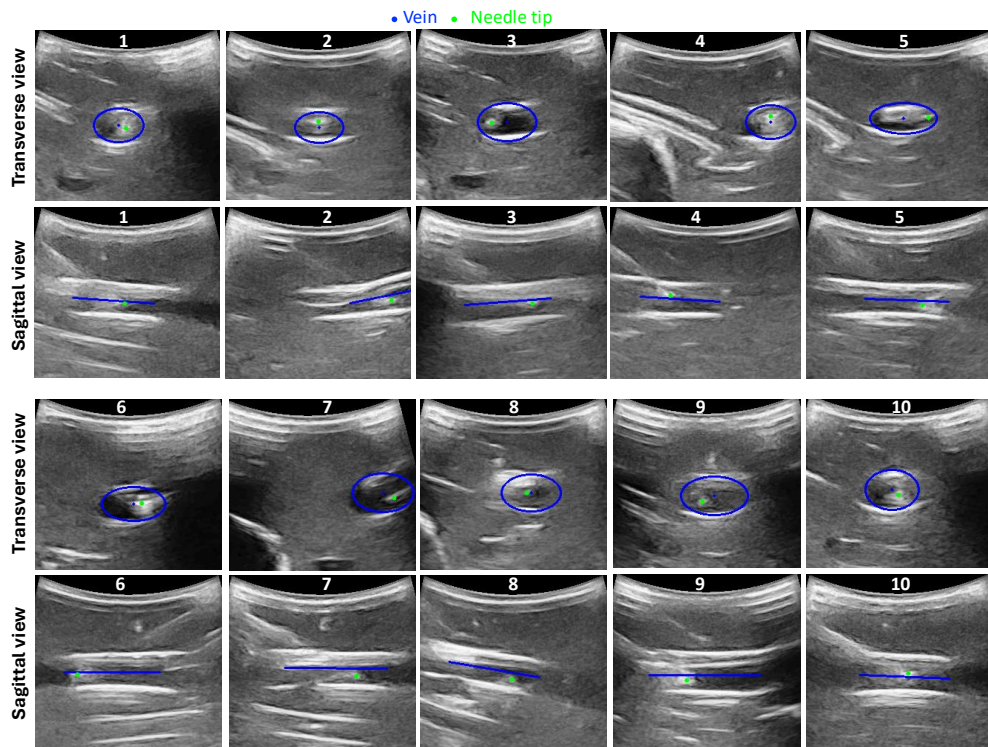


Fig. 9 Expert's annotations on transverse and sagittal ultrasound views acquired with hand-held scanning after insertion

Fig. 9 shows the annotations by the expert in the selected transverse and sagittal ultrasound frame from the recorded ultrasound video during the hand-held scanning of the region. The transverse ultrasound views show that the needle tip was detected inside the IJ vein boundary. The sagittal views confirm that needle did not puncture through the vein and remained closed to the center line of the IJ vein. Further, the expert confirmed that the catheter was successfully inserted. To evaluate, the error was calculated as the distance between needle tip and center-point in the transverse view of the vein. In the sagittal view, the perpendicular distance between needle tip and center-line of vein was also calculated. These distances were initially recorded in *pixel* units and later converted to *mm* using the probe’s scaling factor. Table 4 summarizes these evaluations under the ‘Evaluation via expert’ column.

Table 4 Error between the needle tip and vein center-point or center-line, evaluated with robot kinematics after insertion (Fig. 8) and expert annotations (Fig. 9). Insertion success is marked using ‘✓’ for safe needle insertion, bleeding of blue-color fluid (artery has red-color fluid), and catheter insertion.

Evaluation via →	Error between needle tip and IJ vein’s				Insertion Success		
	center-point (<i>mm</i>)		center-line (<i>mm</i>)		Safe	Blue	Catheter
	Robot	Expert	Robot	Expert	insertion	bleed	insertion
1	1.87	1.66	0.39	0.45	✓	✓	✓
2	3.08	1.24	1.01	1.14	✓	✓	✓
3	6.85	1.24	0.90	0.72	✓	✓	✓
4	0.31	3.25	0.47	0.78	✓	✓	✓
5	5.26	5.09	0.32	0.96	✓	✓	✓
Mean (1-5)	3.47	2.49	0.62	0.63			
S.D. (1-5)	2.61	1.49	0.31	0.29			
6	4.50	2.17	1.15	0.46	✓	✓	✓
7	1.27	2.49	0.25	1.52	✓	✓	✓
8	1.24	2.06	0.80	1.85	✓	✓	✓
9	2.19	1.57	1.38	1.32	✓	✓	✓
10	2.18	2.01	0.31	0.69	✓	✓	✓
Mean (6-10)	2.28	2.06	0.78	1.17			
S.D. (6-10)	1.33	0.29	0.50	0.52			

4 Discussion

We presented experimental phantom results to evaluate vessel centerline reconstruction and needle targeting accuracy. The proposed pipeline and validation study will serve as a foundation for future clinically deployable system. There were also some less-than-ideal performance issues with our experimental goals, which can be explained as follows.

The reconstructed vein exhibited a relatively high mean±S.D. error (Table 3), with two possible explanations. First, the vein has greater compressibility compared to the artery under force-controlled robotic scanning. This compression was not accounted

for in the ground truth (i.e., intra-operative CT scan). Second, we attribute this error to the use of convex ultrasound probe. While linear probes are typically preferred for CVC, we only had access to a convex probe for this study. Nonetheless, these results (mean error of vein and artery combined is 2.15 mm) indicate that the calibrated transformation from ultrasound image to the 3D space preserves the spatial accuracy of the vein and artery without larger deviation, which is critical for identifying the accurate needle entry point.

The needle targeting accuracy (Fig. 8) shows that the needle tip consistently reached near the IJ vein centerline, with average errors of 0.62 mm and 0.78 mm for Exp. 1–5 and 6–10, respectively (Table 4). These values are close to or under the 1 mm threshold used in the needle controller (Section 2.5). However, slightly higher average errors from the vein center could be due to bending of the 150 mm long needle. Still, all errors remained well within the vein’s ground truth radius (3.24 to 6.16 mm).

For expert-evaluated manual scans, the mean \pm SD error from the center-point was $2.49 \pm 1.49\text{ mm}$ and $2.06 \pm 0.29\text{ mm}$ for Exp. 1–5 and 6–10, respectively. The highest error occurred in Exp. 4 and 5, likely due to unavoidable tilting of the needle mechanism. The mean \pm SD error from the center-line was $0.63 \pm 0.29\text{ mm}$ and $1.17 \pm 0.52\text{ mm}$, for these two set of experiments, respectively. In Exp. 6–10, error increased with induced trajectory noise (notably in Exp. 6–9), but decreased again in Exp. 10 due to unpredictable needle bending. Despite such variations, all experiments kept the targeting error within the vein’s radius (3.24 to 6.16 mm), confirming effective insertion. Moreover, for contextual reference, Chen *et al.* [21] reported a positional accuracy of $0.9 \pm 0.29\text{ mm}$ across five needle insertions in a pork phantom.

There are three limitations of the system that can be addressed in future work. First, reducing the needle mechanism’s weight (currently $\sim 4.5\text{ Kg}$) and overall size would enhance its positioning flexibility, which would be needed for obese patients. Second, although needle insertion angles were limited by the geometric constraints of the curved rail coupled with the probe, future designs enabling independent motion of the probe and needle could allow for steeper insertion angles, better aligning with clinical preferences. Lastly, manual marking of the needle tip in ultrasound images during insertion limits real-time capability, so future pipeline will explore automated detection.

5 Conclusion

We have shown that the effective integration of intra-operative planning, anatomical identification, and needle guidance could enable the end-to-end robotic execution of central venous catheterization. To the best of our knowledge, this is the first time a sole depth camera feedback has been used to identify the scanning region, thereby eliminating the need to rely on medical experts or intra-operative CT/MRI scans. Another novelty of this work is the use of force-guided robotic motion to identify the vein and artery based on their compressibility, thereby reducing the reliance on complex ultrasound imaging feedback (multi-class segmentation or Doppler ultrasound). The success of this system can be observed from the successful needle placement with an error below or close to 1 mm . In future, we will use anatomically representative

phantoms [26] or fresh cadavers to further validate the system under more realistic physiological conditions.

Acknowledgements. This work is partially supported by the Agency for Healthcare Research and Quality (AHRQ) under Grant No. 7R18HS029124-03 (previously 5R18HS029124-03), the National Science Foundation (NSF) CAREER Award under Grant No. 2144348, the NSF Future of Work at the Human-Technology Frontier (FW-HTF) Award No. 2222716, the NSF Alan T. Waterman Award No. 2431810, and the Malone Center for Engineering in Healthcare Postdoctoral Fellowship.

References

- [1] Kehagias, E., Galanakis, N., Tsetis, D.: Central venous catheters: Which, when and how. *The British Journal of Radiology* **96**(1151), 20220894 (2023)
- [2] Govindan, S., Snyder, A., Flanders, S.A., Chopra, V.: Peripherally inserted central catheters in the icu: a retrospective study of adult medical patients in 52 hospitals. *Critical care medicine* **46**(12), 1136–1144 (2018)
- [3] Teja, B., Bosch, N.A., Diep, C., Pereira, T.V., Mauricio, P., Sklar, M.C., Sankar, A., Wijeyesundera, H.C., Saskin, R., Walkey, A., *et al.*: Complication rates of central venous catheters: a systematic review and meta-analysis. *JAMA Internal Medicine* **184**(5), 474–482 (2024)
- [4] Ikhsan, M., Tan, K.K., Putra, A.S.: Assistive technology for ultrasound-guided central venous catheter placement. *Journal of Medical Ultrasonics* **45**, 41–57 (2018)
- [5] Biswas, P., Sikander, S., Kulkarni, P.: Recent advances in robot-assisted surgical systems. *Biomedical Engineering Advances* **6**, 100109 (2023)
- [6] Raina, D., Singh, H., Saha, S.K., Arora, C., Agarwal, A., Chandrashekhara, S., Rangarajan, K., Nandi, S.: Comprehensive telerobotic ultrasound system for abdominal imaging: Development and in-vivo feasibility study. In: 2021 International Symposium on Medical Robotics (ISMR), pp. 1–7 (2021). IEEE
- [7] Raina, D., Balakuntala, M.V., Kim, B.W., Wachs, J., Voyles, R.: Coaching a robotic sonographer: Learning robotic ultrasound with sparse expert’s feedback. *IEEE Transactions on Medical Robotics and Bionics* (2024)
- [8] Slocum, A., Bassett, E., Karp, J.M., Langer, R.S., Farokhzad, O.C.: Methods and devices for sensing tissues and tissue compartments. Google Patents. US Patent 8,920,388 (2014)
- [9] Cheng, Z., Davies, B.L., Caldwell, D.G., Mattos, L.S.: Sdop: A smart hand-held device for over puncture prevention during pediatric peripheral intravenous

- catheterization. In: 2018 International Symposium on Medical Robotics (ISMR), pp. 1–6 (2018). IEEE
- [10] Cheng, Z., Davies, B.L., Caldwell, D.G., Mattos, L.S.: A hand-held robot for precise and safe pivc. *IEEE Robotics and Automation Letters* **4**(2), 655–661 (2019)
- [11] Hong, J., Dohi, T., Hashizume, M., Konishi, K., Hata, N.: An ultrasound-driven needle-insertion robot for percutaneous cholecystostomy. *Physics in Medicine & Biology* **49**(3), 441 (2004)
- [12] Neubach, Z., Shoham, M.: Ultrasound-guided robot for flexible needle steering. *IEEE Transactions on Biomedical Engineering* **57**(4), 799–805 (2009)
- [13] Xu, J., Jia, Z.-z., Song, Z.-j., Yang, X.-d., Chen, K., Liang, P.: Three-dimensional ultrasound image-guided robotic system for accurate microwave coagulation of malignant liver tumours. *The International Journal of Medical Robotics and Computer Assisted Surgery* **6**(3), 256–268 (2010)
- [14] Chatelain, P., Krupa, A., Navab, N.: 3d ultrasound-guided robotic steering of a flexible needle via visual servoing. In: 2015 IEEE International Conference on Robotics and Automation (ICRA), pp. 2250–2255 (2015). IEEE
- [15] Zettinig, O., Frisch, B., Virga, S., Esposito, M., Rienmüller, A., Meyer, B., Hengersperger, C., Ryang, Y.-M., Navab, N.: 3d ultrasound registration-based visual servoing for neurosurgical navigation. *International journal of computer assisted radiology and surgery* **12**, 1607–1619 (2017)
- [16] Kojcev, R., Fuerst, B., Zettinig, O., Fotouhi, J., Lee, S.C., Frisch, B., Taylor, R., Sinibaldi, E., Navab, N.: Dual-robot ultrasound-guided needle placement: closing the planning-imaging-action loop. *International journal of computer assisted radiology and surgery* **11**, 1173–1181 (2016)
- [17] Bell, M.A.L., Shubert, J.: Photoacoustic-based visual servoing of a needle tip. *Scientific Reports* **8**, 15519 (2018)
- [18] Gubbi, M.R., Bell, M.A.L.: Deep learning-based photoacoustic visual servoing: Using outputs from raw sensor data as inputs to a robot controller. In: Proceedings of the IEEE International Conference on Robotics and Automation (ICRA) (2021). IEEE
- [19] Cheng, Z., Davies, B.L., Caldwell, D.G., Mattos, L.S.: A venipuncture detection system for robot-assisted intravenous catheterization. In: 2016 6th IEEE International Conference on Biomedical Robotics and Biomechatronics (BioRob), pp. 80–86 (2016). IEEE

- [20] Koskinopoulou, M., Acemoglu, A., Penza, V., Mattos, L.S.: Dual robot collaborative system for autonomous venous access based on ultrasound and bioimpedance sensing technology. In: 2023 IEEE International Conference on Robotics and Automation (ICRA), pp. 4648–4653 (2023). IEEE
- [21] Chen, S., Wang, F., Lin, Y., Shi, Q., Wang, Y.: Ultrasound-guided needle insertion robotic system for percutaneous puncture. *International Journal of Computer Assisted Radiology and Surgery* **16**, 475–484 (2021)
- [22] Kim, C., Chang, D., Petrisor, D., Chirikjian, G., Han, M., Stoianovici, D.: Ultrasound probe and needle-guide calibration for robotic ultrasound scanning and needle targeting. *IEEE Transactions on Biomedical Engineering* **60**(6), 1728–1734 (2013)
- [23] Kosnik, N., Kowalski, T., Lorenz, L., Valacer, M., Sakthi-Velavan, S.: Anatomical review of internal jugular vein cannulation. *Folia Morphologica* **83**(1), 1–19 (2024)
- [24] Teixeira, B., Singh, V., Tamersoy, B., Prokein, A., Kapoor, A.: Automated ct lung cancer screening workflow using 3d camera. In: *International Conference on Medical Image Computing and Computer-Assisted Intervention*, pp. 423–431 (2023). Springer
- [25] Li, X., Chen, H., Qi, X., Dou, Q., Fu, C.-W., Heng, P.-A.: H-denseunet: hybrid densely connected unet for liver and tumor segmentation from ct volumes. *IEEE transactions on medical imaging* **37**(12), 2663–2674 (2018)
- [26] Al-Zogbi, L., Raina, D., Pandian, V., Fleiter, T., Krieger, A.: Robotic ultrasound-guided femoral artery reconstruction of anatomically-representative phantoms. *arXiv preprint arXiv:2503.06795* (2025)